

2421 **Chapter 9**  
2422 **Weak Focusing Synchrotron**

2423 **Abstract** This Chapter introduces to the weak focusing synchrotron, and to the the-  
2424 oretical material needed for the simulation exercises. It begins with a brief reminder  
2425 of the historical context, and continues with beam optics and acceleration techniques  
2426 which the weak synchrotron principle and methods lean on. Regarding the latter, it  
2427 relies on basic charged particle optics and acceleration concepts introduced in the  
2428 previous Chapters, and further addresses the following aspects:

- 2429 - fixed closed orbit,
- 2430 - periodic structure,
- 2431 - periodic motion stability,
- 2432 - optical functions,
- 2433 - synchrotron motion,
- 2434 - depolarizing resonances.

2435 The simulation of weak synchrotrons only require a very limited number of optical  
2436 elements; actually two are enough: DIPOLE or BEND to simulate combined function  
2437 dipoles, and DRIFT to simulate straight section. A third one CAVITE, is required  
2438 for acceleration. Particle monitoring requires keywords introduced in the previous  
2439 Chapters, including FAISCEAU, FAISTORE, possibly PICKUPS, and some others.  
2440 Spin motion computation and monitoring resort to SPNTRK, SPNPRT, FAISTORE.  
2441 Optics matching and optimization use FIT[2]. SYSTEM again is used to shorten the  
2442 input data files.

2443 **Notations used in the Text**

$B; \mathbf{B}, B_{x,y,s}$	field value; field vector, its components in the moving frame
$B\rho = p/q; B\rho_0$	particle rigidity; reference rigidity
$C; C_0$	orbit length, $C = 2\pi R + \left[ \begin{array}{l} \text{straight} \\ \text{sections} \end{array} \right]$ ; reference, $C_0 = C(p = p_0)$
$E$	particle energy
EFB	Effective Field Boundary
$f_{\text{rev}}, f_{\text{rf}}$	revolution and accelerating voltage frequencies
$h$	RF harmonic number, $h = f_{\text{rf}}/f_{\text{rev}}$
$m; m_0; M$	mass, $m = \gamma m_0$ ; rest mass; in units of MeV/c <sup>2</sup>
$n = \frac{\rho}{B} \frac{dB}{d\rho}$	focusing index
$\mathbf{p}; p; p_0$	momentum vector; its modulus; reference
$P_i, P_f$	polarization, initial, final
$q$	particle charge
$r, R$	orbital radius ; average radius, $R = C/2\pi$
$s$	path variable
$v$	particle velocity
$V(t); \hat{V}$	oscillating voltage; its peak value
2444 $x, x', y, y'$	horizontal and vertical coordinates in the moving frame
$\alpha$	momentum compaction, or trajectory deviation
$\beta = v/c; \beta_0; \beta_s$	normalized particle velocity; reference; synchronous
$\beta_u$	betatron functions ( $u : x, y, Y, Z$ )
$\gamma = E/m_0$	Lorentz relativistic factor
$\Delta p, \delta p$	momentum offset
$\varepsilon$	wedge angle
$\varepsilon_u$	Courant-Snyder invariant ( $u : x, r, y, l, Y, Z, s$ , etc.)
$\epsilon_R$	strength of a depolarizing resonance
$\mu_u$	betatron phase advance, $\mu_u = \int_{\text{period}} ds/\beta_u(s)$ ( $u : x, y, Y, Z$ )
$\nu_u$	wave number, radial, vertical, synchrotron ( $u : x, y, Y, Z, l$ )
$\rho$	curvature radius
$\phi; \phi_s$	particle phase at voltage gap; synchronous phase
$\phi_u$	betatron phase advance, $\phi_u = \int ds/\beta_u$ ( $u : x, y, Y, \text{ or } Z$ )
$\varphi$	spin angle to the vertical axis

2445 **Introduction**

2446 The synchrotron is an outcome of the mid-1940s longitudinal phase focusing syn-  
 2447 chronous acceleration concept [1, 2]. In its early version, transverse beam stability  
 2448 in the synchrotron during the thousands of turns that the acceleration lasts was based  
 2449 on the technique known at the time: weak focusing, as in the cyclotron and in the be-  
 2450 tatron. An existing betatron was used to first demonstrate phase-stable synchronous

2451 acceleration with slow variation of the magnetic field, on a fixed orbit, in 1946 [3],  
 2452 - closely following the demonstration of the principle of phase focusing using a  
 2453 fixed-field cyclotron [4].

2454 Phase focusing states that stability of the longitudinal motion, longitudinal focus-  
 2455 ing, is obtained if particles in a bunch, which have a natural energy spread, arrive  
 2456 at the accelerating gap in the vicinity of a proper phase of the oscillating voltage,  
 2457 the synchronous phase; if this condition is fulfilled the bunch stays together, in the  
 2458 vicinity of the latter, during acceleration. Synchrotrons operate in general in a non-  
 2459 isochronous regime: the revolution period changes with energy; as a consequence,  
 2460 in order to maintain an accelerated bunch on the synchronous phase, the RF voltage  
 2461 frequency, which satisfies  $f_{rf} = h f_{rev}$ , has to change continuously from injection to  
 2462 top energy. The reference orbit in a synchrotron is maintained at constant radius by  
 2463 ramping the guiding field in the main dipoles in synchronism with the acceleration,  
 2464 as in the betatron [5].

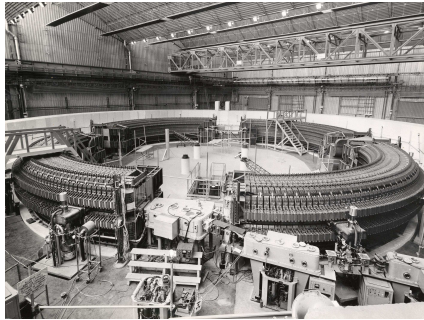


**Fig. 9.1** Saturne I at Saclay [6], a 3 GeV, 4-period, 68.9 m circumference, weak focusing synchrotron, constructed in 1956-58. The injection line can be seen in the foreground, injection is from a 3.6 MeV Van de Graaff (not visible)

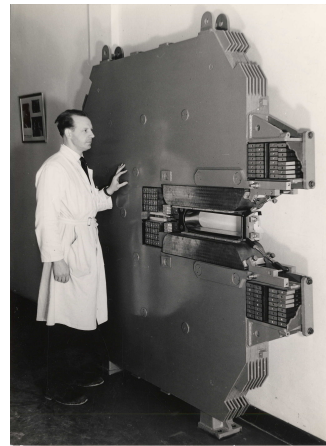


**Fig. 9.2** A slice of Saturne I dipole [7]. The slight gap tapering is hardly visible (increasing outward), it determines the weak index condition  $0 < n < 1$

2465 The synchrotron concept allowed the highest energy reach by particle accelerators  
 2466 at the time, it led to the construction of a series of proton rings with increasing  
 2467 energy [8]: 1 GeV at Birmingham (1953), 3.3 GeV at the Cosmotron (Brookhaven  
 2468 National Laboratory, 1953-1969), 6.2 GeV at the Bevatron (Berkeley, 1954-1993),  
 2469 10 GeV at the Synchro-Phasotron (JINR, Dubna, 1957-2003), and a few additional  
 2470 ones in the late 1950s well into the era of the concept which would essentially  
 2471 dethrone the weak focusing method and its quite bulky rings of magnets which were  
 2472 a practical limit to further increase in energy<sup>1</sup>: the strong focusing synchrotron (the

<sup>1</sup> The story has it that it is possible to ride a bicycle in the vacuum chamber of Dubna's Synchro-Phasotron.

2473 object of Chapter 10). The general layout of these first weak focusing synchrotrons  
 2474 included straight sections (often 4, Fig. 9.1), which allowed insertion of injection  
 2475 (Fig. 9.1) and extraction systems, accelerating cavities, orbit correction and beam  
 2476 monitoring equipment.

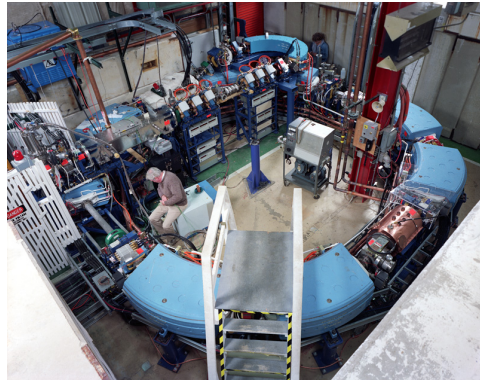


**Fig. 9.3** Left: Loma Linda University medical synchrotron, during commissioning in 1989 at the Fermilab National Laboratory where it was designed and constructed [9]

2477 The next decades following the invention of the synchrotron saw applications in  
 2478 many fields of science including fixed-target nuclear physics for particle discovery,  
 2479 material science, medicine, industry. Its technological simplicity still makes it an  
 2480 appropriate technology today in low energy beam application when relatively low  
 2481 current is not a concern, as in the hadrontherapy application (Fig. 9.3) [10, 11]: it  
 2482 essentially requires a single type of a simple dipole magnet, an accelerating gap, some  
 2483 command-control instrumentation, whereas it procures greater beam manipulation  
 2484 flexibilities compared to (synchro-)cyclotrons.

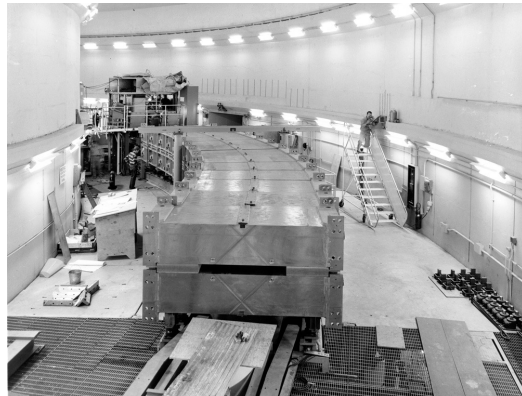


**Fig. 9.4** The ZGS at Argonne during construction. A 12 GeV, 8-dipole, 4-period, 172 m circumference, wedge focusing synchrotron. The two persons inside and outside the ring, in the background, give an idea of the size of the magnets

2485 *Polarized beams*

2486 The availability of polarized proton sources allowed the acceleration of polarized  
 2487 beams to high energy. The possibility was considered from the early times at Argonne  
 2488 ZGS (Zero-Gradient Synchrotron), a 12 GeV weak focusing synchrotron operated  
 2489 over 1964-1979 [12] (Fig. 9.4). Up to 70% polarization transmission through the  
 2490 synchrotron was achieved, for the first time in a synchrotron<sup>2</sup> and reaching multi-  
 2491 GeV energy in 1973. Polarization preservation techniques included harmonic orbit  
 2492 correction, tune jump at strongest depolarizing resonances (Fig. 9.14), four years  
 2493 after the ZGS startup. Beams were accelerated up to 17 GeV with substantial po-  
 2494 larization maintained [13]. Experiments were performed to assess the possibility of  
 2495 polarization transmission in strong focusing synchrotrons, and polarization lifetime  
 2496 in colliders [14]. Acceleration of polarized deuteron was achieved in the late 1970s,  
 2497 when sources were made available [15].

2498 **9.1 Basic Concepts and Formulae**

2499 The synchrotron is based on two key principles. On the one hand, a slowly varying  
 2500 magnetic field to maintain a constant orbit during acceleration,

$$B(t) \times \rho = p(t)/q, \quad \rho = \text{constant}, \quad (9.1)$$

2501 with  $p(t)$  the particle momentum and  $\rho$  the bending radius in the dipoles. On the other  
 2502 hand, on synchronous acceleration for longitudinal phase stability. In a regime where  
 2503 the velocity change with energy cannot be ignored (non-ultrarelativistic particles),  
 2504 the latter requires a modulation of the accelerating voltage frequency so to satisfy

$$f_{RF}(t) = hf_{rev}(t) \quad (9.2)$$

2505 Synchronism between accelerating voltage oscillation and the revolution motion  
 2506 keeps the bunch on the synchronous phase at traversal of the accelerating gaps.  
 2507 Synchronous acceleration is technologically simpler in the case of electrons, as  
 2508 frequency modulation is unnecessary beyond a few MeV; for instance, from  $v/c =$   
 2509  $0.9987$  at 10 MeV to  $v/c \rightarrow 1$  the relative change in revolution frequency amounts  
 2510 to  $\delta f_{rev}/f_{rev} = \delta\beta/\beta < 0.0013$ .

2511 These are two major evolutions compared to the cyclotron, where, instead, the  
 2512 magnetic field is fixed - the reference orbit spirals out, and, by virtue of the isochro-  
 2513 nism of the orbits, the oscillating voltage frequency is fixed as well.

2514 A fixed orbit reduces the radial extent of individual guiding magnets, allowing a  
 2515 ring structure comprised of a circular string of dipoles. For the sake of comparison:  
 2516 a synchrocyclotron instead uses a single, massive dipole; increased energy requires  
 2517 increased radial extent of the magnet to allow for the greater bending field integral

---

<sup>2</sup> Polarized beam had been accelerated in cyclotrons, at earlier times.

2518 (*i.e.*,  $\oint B dl = 2\pi R_{max} \hat{B} = p_{max}/q$ ), thus a volume of iron increasing more than  
 2519 quadratically with bunch rigidity.

2520 One or the other of the weak index ( $-1 < k < 0$ , Sect. 4.2.2) and/or wedge  
 2521 focusing (Sect. 18.3.1) are used in weak focusing synchrotrons. Transverse stability  
 2522 was based on the latter at Argonne ZGS (Zero-Gradient Synchrotron: the main  
 2523 magnet had no field index); ZGS accelerated polarized proton beams, weak focusing  
 2524 resulted in weak depolarizing resonances, an advantage in that matter [14].

2525 Due to the necessary ramping of the field in order to maintain a constant orbit,  
 2526 the synchrotron is a pulsed accelerator, the acceleration is cycled, from injection to  
 2527 top energy, repeatedly. The repetition rate of the acceleration cyclic depends on the  
 2528 type of power supply. If the ramping uses a constant electromotive force ( $E=V+ZI$   
 2529 is constant), then

$$B(t) \propto (1 - e^{-\frac{t}{\tau}}) = 1 - \left[ 1 - \left(\frac{t}{\tau}\right) + \left(\frac{t}{\tau}\right)^2 - \dots \right] \approx \frac{t}{\tau} \quad (9.3)$$

2530 essentially linear. In that case  $\dot{B} = dB/dt$  does not exceed a few Tesla/second, thus the  
 2531 repetition rate of the acceleration cycle if of the order of a Hertz. If instead the magnet  
 2532 winding is part of a resonant circuit (with typically 10 ~ 60 Hz eigenfrequency) the  
 2533 field oscillate,

$$B(t) = B_0 + \frac{\hat{B}}{2}(1 - \cos \omega t) \quad (9.4)$$

2534 so that, in the interval of half a voltage repetition period (*i.e.*,  $t : 0 \rightarrow \pi/\omega$ ) the  
 2535 field increases from an injection threshold value to a maximum value at highest  
 2536 rigidity,  $B(t) : B_0 \rightarrow B_0 + \hat{B}$ . The latter determines the highest achievable energy:  
 2537  $\hat{E} = pc/\beta = q\hat{B}\rho c/\beta$ . The repetition rate with resonant magnet cycling can reach  
 2538 a few tens of Hertz, a species known as “rapid-cycling” synchrotrons. In both cases  
 2539 anyway B imposes its law and the other quantities comprising the acceleration cycle  
 2540 (RF frequency in particular) will follow B(t).

2541 For the sake of comparison: in a synchrocyclotron the field is constant, thus  
 2542 acceleration can be cycled as fast as the swing of the voltage frequency allows  
 2543 (hundreds of Hz are common practice); assume a conservative 10 kVolts per turn,  
 2544 thus of the order of 10,000 turns to 100 MeV, with velocity  $0.046 < v/c < 0.43$   
 2545 from 1 to 100 MeV, proton. Take  $v \approx 0.5c$  to make it simple, an orbit circumference  
 2546 below 30 meter, thus the acceleration takes of the order of  $10^4 \times C/0.5c \approx$ ms range,  
 2547 potentially a repetition rate in kHz range, more than an order of magnitude beyond  
 2548 the reach of a rapid-cycling pulsed synchrotron.

### 2549 9.1.1 Periodic Stability

2550 This section introduces the various components of the transverse focusing and the  
 2551 conditions for periodic stability in a weak focusing synchrotron. It builds on material  
 2552 introduced in Chap. 4, Classical Cyclotron, and on Ref. [16].

2553 **9.1.1.1 Closed orbit**

2554 The concept is found in the betatron, which accelerates particles on a constant orbit  
 2555 (Chap. 7). The closed orbit is fixed, and maintained during acceleration by ensuring  
 2556 that the relationship Eq. 9.1 is satisfied. In a perfect ring, the closed orbit is along an  
 2557 arc in the bending magnets and straight along the drifts, Fig. 9.5.

2558 Particle motion is defined in a moving frame (O;s,x,y) whose origin coincides  
 2559 with the location of an ideal particle following the reference orbit. The moving frame  
 2560 s axis is tangent to the reference orbit, its transverse horizontal axis x is normal to  
 2561 the s axis, its vertical axis y is normal to the (s,x) plane (Fig. 4.8, Sect. 4.2.2).

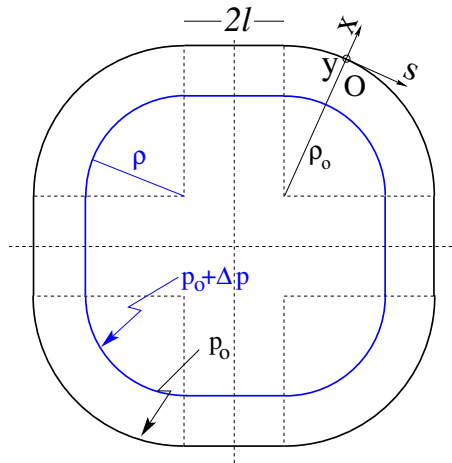


**Fig. 9.5** A  $2\pi/4$  axially symmetric structure with four drift spaces. Orbit length on reference momentum  $p_0$  is  $C = 2\pi\rho_0 + 8l$ . (O;s,x,y) is the moving frame, along the reference orbit. The orbit for momentum  $p = p_0 + \Delta p$  ( $\Delta p < 0$ , here) is at constant distance  $\Delta x = \frac{\rho_0}{1-n} \frac{\Delta p}{p_0} = \frac{R}{(1+k)(1-n)} \frac{\Delta p}{p_0}$  from the reference orbit

2562 **9.1.1.2 Transverse Focusing**

2563 Radial motion stability around a reference closed orbit in an axially symmetric dipole  
 2564 field requires a field index (Sect. 4.2.2),

$$n = -\frac{\rho_0}{B_0} \left. \frac{\partial B_y}{\partial \rho} \right|_{x=0, y=0} \quad (9.5)$$

2565 a quantity evaluated on the reference arc in the dipoles, satisfying the weak focusing  
 2566 condition

$$0 < n < 1 \quad (9.6)$$

2567 This condition can be obtained with a tapered gap (Fig. 9.2) causing the magnetic  
 2568 field to decrease slowly with radius. Note the sign convention here, the cyclotron

2569 uses the opposite sign (Eq. 4.10). This condition holds regardless of the presence of  
 2570 drifts or not. Adding drift spaces between the dipoles, the reference orbit is comprised  
 2571 of arcs of radius  $\rho_0$  in the magnets, and straight segments along the drift spaces that  
 2572 connect these arcs. This requires defining two radii, namely,

- 2573 (i) the magnet curvature radius  $\rho_0$ ,  
 2574 (ii) an average radius  $R = C/2\pi = \rho_0 + Nl/\pi$  (with  $C$  the length of the reference  
 2575 closed orbit and  $2l$  the drift length) (Fig. 9.5) which also writes

$$R = \rho_0(1 + k), \quad k = \frac{Nl}{\pi\rho_0} \quad (9.7)$$

2576 Adding drift spaces decreases the average focusing around the ring.

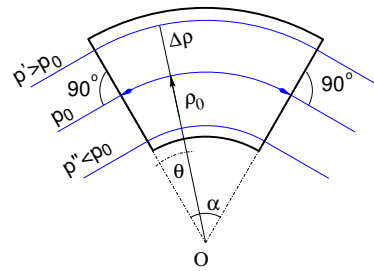


**Fig. 9.6** In a sector dipole with radial index  $n \neq 0$ , closed orbits follow arcs of constant field. A closed orbit at  $\rho_0 + \Delta\rho$  follows an arc of radius  $\rho_0 + \Delta\rho$ ,  $\Delta\rho = \Delta\rho/(1+n)qB_0$

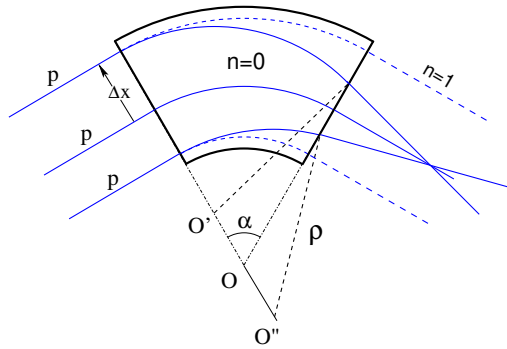
### 2577 Geometrical focusing

2578 The limit  $n \rightarrow 1$  of the transverse motion stability domain corresponds to a cancel-  
 2579 lation of the geometrical focusing (Fig. 9.7): in a constant field dipole (radial field  
 2580 index  $n=0$ ) the longer (respectively shorter) path in the magnetic field for parallel  
 2581 trajectories entering the magnet at greater (respectively smaller) radius result in  
 2582 convergence. This effect is cancelled, *i.e.*, the deviation is the same whatever the  
 2583 entrance radius, if the curvature center is made independent of the entrance radius:  
 2584  $OO' = 0$ ,  $O''O = 0$ . This occurs if trajectories at an outer (inner) radius experience a  
 2585 smaller (greater) field such as to satisfy  $BL = B\rho\alpha = C^{st}$ . Differentiating  $B\rho = C^{st}$   
 2586 gives  $\frac{\Delta B}{B} + \frac{\Delta\rho}{\rho} = 0$ , with  $\Delta\rho = \Delta x$ , so yielding  $n = -\frac{\rho_0}{B_0} \frac{\Delta B}{\Delta x} = 1$ . The focal distance

2587 associated with the curvature is (Eq. 4.12 with  $R = \rho_0$ )  $f = \frac{\rho_0^2}{L}$ . Optical drawbacks  
 2588 of the weak focusing method include the weakness of the focusing and the absence  
 2589 of independent radial and axial focusing.



**Fig. 9.7** Geometrical focusing: in a sector dipole with focusing index  $n = 0$ , parallel incoming rays of equal momenta experience the same curvature radius  $\rho$ , they exit converging, as a result of the longer path of outer trajectories in the field, compared to inner ones. An index value  $n=1$  cancels that effect: rays exit parallel



2590 *Wedge Focusing*

2591 Entrance and exit wedge angles may be used to ensure transverse focusing: opening  
 2592 the magnetic sector increases the horizontal focusing (and decreases the vertical  
 2593 focusing); closing the magnetic sector has the reverse effect (Sect. 18.3.1). In a point  
 2594 transform approximation, at the wedge the trajectory undergoes a local deviation  
 2595 proportional to the distance to the optical axis, namely,

$$\Delta x' = \frac{\tan \varepsilon}{\rho_0} \Delta x, \quad \Delta y' = -\frac{\tan(\varepsilon - \psi)}{\rho_0} \Delta y \quad (9.8)$$

2596  $\psi$  is a correction for the fringe field extent (Eq. 18.20), an effect on the vertical  
 2597 focusing of the first order in the coordinates (it is a second order effect horizontally).

2598 Profiling the magnet gap in order to adjust the focal distance complicates the  
 2599 magnet; a parallel gap,  $n = 0$ , makes it simpler, for that reason edge focusing may  
 2600 be preferred. Wedge vertical focusing in the ZGS ( $\varepsilon > 0$ ) was at the expense of  
 2601 horizontal geometrical focusing (Fig. 9.6). This was an advantage though, for the  
 2602 acceleration of polarized beams, as radial field components (which are responsible for  
 2603 depolarization) were only met at the EFBs of the eight main dipoles [13]. Preserving  
 2604 beam polarization at high energy required tight control of the tunes, and this was  
 2605 achieved by, in addition, pole face windings at the ends of the dipoles [17, 18];  
 2606 these coils were pulsed to control the amplitude detuning, resulting in a control  
 2607 of the tunes at 0.01 level; they also compensated eddy current induced sextupole  
 2608 perturbations which affected the vertical tune.

2609 **9.1.1.3 Periodic stability, betatron motion**

2610 The first order differential equations of motion in the moving frame (Fig. 9.5) derive  
 2611 from the Lorentz equation [16]

$$\frac{d\mathbf{mv}}{dt} = q\mathbf{v} \times \mathbf{B} \Rightarrow m \frac{d}{dt} \left\{ \begin{array}{c} \frac{ds}{dt} \mathbf{s} \\ \frac{dx}{dt} \mathbf{x} \\ \frac{dy}{dt} \mathbf{y} \end{array} \right\} = q \left\{ \begin{array}{c} (\frac{dx}{dt} B_y - \frac{dy}{dt} B_x) \mathbf{s} \\ -\frac{ds}{dt} B_y \mathbf{x} \\ \frac{ds}{dt} B_x \mathbf{y} \end{array} \right\} \quad (9.9)$$

2612 Introduce the field index  $n = -\frac{\rho_0}{B_0} \frac{\partial B_y}{\partial x}$  evaluated on the reference orbit, with  $B_0 =$   
 2613  $B_y(\rho_0, y = 0)$ ; assume transverse stability:  $0 < n < 1$ . Taylor expansion of the  
 2614 transverse field components in the moving frame write

$$B_y(\rho) = B_y(\rho_0) + x \left. \frac{\partial B_y}{\partial x} \right|_{\rho_0} + \mathcal{O}(x^2) \approx B_y(\rho_0) - n \frac{B_y}{\rho_0} \Big|_{\rho_0} x = B_0(1 - n \frac{x}{\rho_0})$$

$$B_x(0 + y) = \underbrace{B_x(0)}_{=0} + y \underbrace{\left. \frac{\partial B_x}{\partial y} \right|_{\rho_0}}_{=\frac{\partial B_y}{\partial x}} (+ \text{higher order in } y) \approx -n \frac{B_0}{\rho_0} y \quad (9.10)$$

2615 Introduce in addition  $ds \approx v dt$ , Eqs. 9.9, 9.10 lead to the differential equations of  
 2616 motion in a dipole field

$$\frac{d^2 x}{ds^2} + \frac{1-n}{\rho_0^2} x = 0, \quad \frac{d^2 y}{ds^2} + \frac{n}{\rho_0^2} y = 0 \quad (9.11)$$

2617 It results that, in an S-periodic structure comprised of gradient dipoles, wedges  
 2618 and drift spaces, the differential equation of motion takes the general form of Hill's  
 2619 equation, a second order differential equation with periodic coefficient, namely (with  
 2620  $u$  standing for  $x$  or  $y$ ),

$$\left\{ \begin{array}{l} \frac{d^2 u}{ds^2} + K_u(s)u = 0 \\ K_u(s+S) = K_u(s) \end{array} \right. \quad \text{with} \quad \left\{ \begin{array}{l} \text{in dipoles : } \begin{cases} K_x = (1-n)/\rho_0^2 \\ K_y = n/\rho_0^2 \end{cases} \\ \text{at a wedge : } K_{\frac{y}{x}} = \pm(\tan \varepsilon)/\rho_0 \\ \text{in drift spaces : } K_x = K_y = 0 \end{array} \right. \quad (9.12)$$

2621  $K_u(s)$  is S-periodic,  $S = 2\pi R/N$  ( $S = C/4$  for instance in a 4-periodic ring,  
 2622 Figs. 9.1, 9.5). G. Floquet has established [19] that the two independent solutions of  
 2623 Hill's second order differential equation have the form [16]

$$\left| \begin{array}{l} u_1(s) = \sqrt{\beta_u(s)} e^{i \int_0^s \frac{ds}{\beta_u(s)}} \\ du_1(s)/ds = \frac{i - \alpha_u(s)}{\beta_u(s)} u_1(s) \end{array} \right. \quad \text{and} \quad \left| \begin{array}{l} u_2(s) = u_1^*(s) \\ du_2(s)/ds = du_1^*(s)/ds \end{array} \right. \quad (9.13)$$

2624 wherein  $\beta_u(s)$  and  $\alpha_u(s) = -\beta'_u(s)/2$  are S-periodic functions, from what it results  
 2625 that

$$u_{\frac{1}{2}}(s+S) = u_{\frac{1}{2}}(s) e^{\pm i \mu_u} \quad (9.14)$$

2626 wherein

$$\mu_u = \int_{s_0}^{s_0+S} \frac{ds}{\beta_u(s)} \tag{9.15}$$

2627 is the betatron phase advance over a period. A real solution of Hill's equation  
 2628 is the linear combination  $A u_1(s) + A^* u_2^*(s)$ . With  $A = \frac{1}{2} \sqrt{\varepsilon_u/\pi} e^{i\phi}$  following  
 2629 conventional notations, the general solution of Eq. 9.12 then writes

$$\begin{cases} u(s) = \sqrt{\beta_u(s)\varepsilon_u/\pi} \cos\left(\int \frac{ds}{\beta_u} + \phi\right) \\ u'(s) = -\sqrt{\frac{\varepsilon_u/\pi}{\beta_u(s)}} \sin\left(\int \frac{ds}{\beta_u} + \phi\right) + \alpha_u(s) \cos\left(\int \frac{ds}{\beta_u} + \phi\right) \end{cases} \tag{9.16}$$

2630 An invariant of the motion is

$$\frac{1}{\beta_u(s)} [u^2 + (\alpha_u(s)u + \beta_u(s)u')^2] = \frac{\varepsilon_u}{\pi} \tag{9.17}$$

2631 known as the Courant-Snyder invariant. At a given azimuth  $s$  of the periodic struc-  
 2632 ture the observed turn-by-turn motion lies on that ellipse (Fig. 9.8). The form and  
 2633 inclination of the ellipse depend on the observation azimuth  $s$  via the respective local  
 2634 values of  $\alpha_u(s)$  and  $\beta_u(s)$ , but its surface  $\varepsilon_u$  is invariant. Motion along the ellipse  
 2635 is clockwise, as can be figured from Eq. 9.16 considering an observation azimuth  
 $s$  where the ellipse is upright,  $\alpha_u(s) = 0$ . In an N-periodic ring, the phase advance

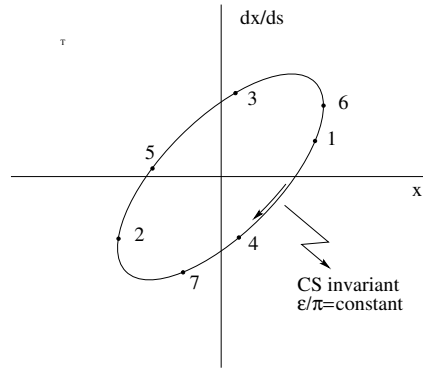


**Fig. 9.8** Courant-Snyder invariant and turn-by-turn harmonic motion along the invariant, observed at some azimuth  $s$ . The form of the ellipse depends on the observation azimuth  $s$  but its surface  $\varepsilon_u$  is invariant

2636 over a turn (from one location to the next on the ellipse in Fig. 9.8) is  
 2637

$$\int_{s_0}^{s_0+NS} \frac{ds}{\beta_u(s)} = N \int_{\text{period}} \frac{ds}{\beta_u(s)} = N\mu_u \tag{9.18}$$

2638 *Weak focusing approximation*

2639 In the case of a cylindrically symmetric structure, a sinusoidal motion is the exact  
 2640 solution of the first order differential equations of motion (Eqs. 4.14, 4.15, Classical  
 2641 Cyclotron Chapter). In that case the latter have a constant (s-independent) coefficient,  
 2642  $K_x = (1 - n)/R_0^2$  and  $K_y = n/R_0^2$ , respectively. Adding drift spaces results in Hill's  
 2643 differential equation with periodic coefficient  $K(s + S) = K(s)$  (Eq. 9.12), and in a  
 2644 pseudo harmonic solution (Eq. 9.16). Due to the weak focusing the beam envelope  
 2645 is only weakly modulated (see below), thus so is  $\beta_u(s)$ . In a practical manner, the  
 2646 modulation of  $\beta_u(s)$  does not exceed a few percent, this justifies introducing the  
 2647 average value  $\bar{\beta}_u$  to approximate the phase advance by

$$\int_0^s \frac{ds}{\beta_u(s)} \approx \frac{s}{\bar{\beta}_u} = \nu_u \frac{s}{R} \quad (9.19)$$

2648 The right equality is obtained by applying this approximation to the the phase advance  
 2649 per period (Eq. 9.15), namely  $\mu_u = \int_{s_0}^{s_0+S} \frac{ds}{\beta_u(s)} \approx S/\bar{\beta}_u$ , and introducing the wave  
 2650 number of the N-period optical structure

$$\nu_u = \frac{N\mu_u}{2\pi} = \frac{\text{phase advance over a turn}}{2\pi} \quad (9.20)$$

2651 so that

$$\bar{\beta}_u = \frac{R}{\nu_u} \quad (9.21)$$

2652 Substituting in Eq. 9.16 yields the approximate solution

$$\begin{cases} u(s) \approx \sqrt{\beta_u(s)\varepsilon_u/\pi} \cos\left(\nu_u \frac{s}{R} + \phi\right) \\ u'(s) = -\sqrt{\frac{\varepsilon_u/\pi}{\beta_u(s)}} \sin\left(\nu_u \frac{s}{R} + \phi\right) + \alpha_u(s) \cos\left(\nu_u \frac{s}{R} + \phi\right) \end{cases} \quad (9.22)$$

2653 In this approximation, the differential equations of motion (Eq. 9.12) can be expressed  
 2654 under the form

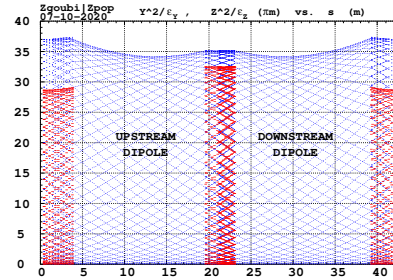
$$\frac{d^2x}{ds^2} + \frac{\nu_x^2}{R^2}x = 0, \quad \frac{d^2y}{ds^2} + \frac{\nu_y^2}{R^2}y = 0 \quad (9.23)$$

2655 *Beam envelopes*

2656 The beam envelope  $\hat{u}(s)$  (with  $u$  standing for  $x$  or  $y$ ) is determined by the particle of  
 2657 maximum invariant  $\varepsilon_u/\pi$ , it is given by

$$\pm \hat{u}(s) = \pm \sqrt{\beta_u(s)\varepsilon_u/\pi} \quad (9.24)$$

**Fig. 9.9** Excursion of a particle along a 43 m long cell, over many turns. The extrema of this motion tangent the envelopes, respectively  $\pm (\beta_x(s) \varepsilon_x / \pi)^{1/2}$ , horizontal (red), and  $\pm (\beta_y(s) \varepsilon_y / \pi)^{1/2}$ , vertical (blue), at all  $s$ . Envelopes are symmetric with respect to  $s = 21.5$  m, a consequence of that very symmetry of the cell

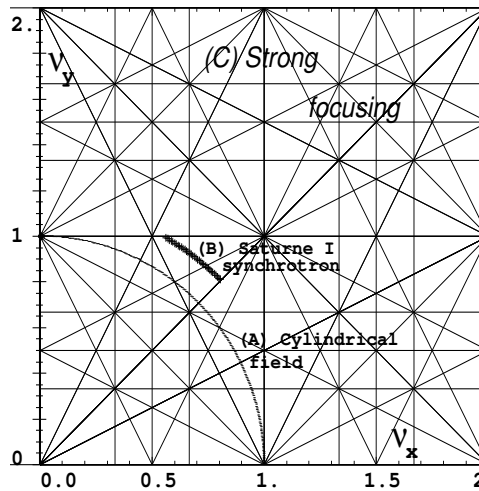


2658 As  $\beta_u(s)$  is S-periodic, so is the envelope,  $\hat{u}(s+S) = \hat{u}(s)$ . In a cell with symmetries,  
 2659 beam envelopes feature the same symmetries, as in Fig. 9.9 for instance: a symmetry  
 2660 with respect to the center of the cell; envelop extrema are at azimuth  $s$  of  $\beta_u(s)$   
 2661 extrema, where  $\alpha_u = 0$  as  $\beta'_u = -2\alpha_u$ .

2662 *Working point*

2663 The “working point” of the synchrotron is the wave number couple  $(\nu_x, \nu_y)$  at which  
 2664 the accelerator is operated, it fully characterizes the focusing. In a structure with  
 2665 cylindrical symmetry  $\nu_x = \sqrt{1-n}$  and  $\nu_y = \sqrt{n}$  (Eq. 4.16) so that  $\nu_x^2 + \nu_y^2 = 1$ : when  
 2666 the radial field index  $n$  is changed the working point stays on a circle of radius 1 in  
 the stability diagram (or “tune diagram”, Fig. 9.10). If drift spaces are added, from

**Fig. 9.10** Location of the working point in the tune diagram, in case of (A) field with revolution symmetry, on a circle of radius 1; (B) sector field with index + drift spaces, on a circle of radius  $(\sqrt{R/\rho_0})$ . Case (C) is for strong focusing,  $(|n| \gg 1)$ ,  $\nu_x$  and  $\nu_y$  are large



2667 the linear approximation (Eqs. 9.11, 9.12) it comes

$$v_x = \sqrt{(1-n)\frac{R}{\rho_0}}, \quad v_y = \sqrt{n\frac{R}{\rho_0}}, \quad v_x^2 + v_y^2 = \frac{R}{\rho_0} \quad (9.25)$$

thus the working point is located on the circle of radius  $\sqrt{R/\rho_0} > 1$ . Tunes can not exceed the limits

$$0 < \nu_{x,y} < \sqrt{R/\rho_0}$$

2668 Horizontal and vertical focusing are not independent (Eq. 9.12): if  $\nu_x$  increases then  
 2669  $\nu_y$  decreases and reciprocally. This is a lack of flexibility which the advent of strong  
 2670 focusing will overcome by providing two knobs allowing separate adjustment of the  
 2671 tunes.

### 2672 Off-momentum orbits

In a dipole with field index  $n = -\frac{\rho_0}{B_0} \frac{\partial B_y}{\partial \rho}$ , orbits different momenta  $p = p_0 + \Delta p$  are concentric (Fig. 9.6), distant (after Eq. 4.18)

$$\Delta x = \frac{\rho_0}{1-n} \frac{\Delta p}{p_0}$$

2673 from the reference orbit. Introduce now the geometrical radius  $R = (1+k)\rho_0$  (Eq. 9.7)  
 2674 to account for the added drifts, this gives

$$\frac{\Delta x}{\Delta p/p_0} \equiv \frac{\Delta R}{\Delta p/p_0} = \frac{R}{(1-n)(1+k)} \quad (9.26)$$

2675 Thus the chromatic dispersion of the orbits, the dispersion function

$$D = \frac{\Delta x}{\Delta p/p_0} = \frac{R}{(1-n)(1+k)}, \quad \text{constant} \quad (9.27)$$

2676 an  $s$ -independent quantity: in a structure with axial symmetry, comprising drift  
 2677 sections (Fig. 9.5) or not (classical and AVF cyclotrons for instance), the ratio  
 2678  $\frac{\Delta x}{\rho_0 \Delta p/p_0}$  is independent of the azimuth  $s$ , the distance of a chromatic orbit to the  
 2679 reference orbit is constant around the ring.

2680 Given that  $n < 1$ ,

- 2681 - higher momentum orbits,  $p > p_0$ , have a greater radius,
- 2682 - lower momentum orbits,  $p < p_0$ , have a smaller radius.

### 2683 Chromatic orbit length

2684 In an axially symmetric structure the difference in closed orbit length  $\Delta C = 2\pi\Delta R$   
 2685 resulting from the difference in momentum arises in the dipoles, as all orbits are

2686 parallel in the drifts (Fig. 9.5). Hence, from Eq. 9.26, the relative closed orbit  
 2687 lengthening factor, “momentum compaction”

$$\alpha = \frac{\Delta C}{C} / \frac{\Delta p}{p_0} \equiv \frac{\Delta R}{R} / \frac{\Delta p}{p_0} = \frac{1}{(1-n)(1+k)} \approx \frac{1}{v_x^2} \quad (9.28)$$

2688 with  $k = Nl/\pi\rho_0$  (Eq. 9.7). Note that the relationship  $\alpha \approx 1/v_x^2$  between momentum  
 2689 compaction and horizontal wave number established for a revolution symmetry  
 2690 structure (Eq. 4.20) still holds when adding drifts.

2691 **9.1.1.4 Longitudinal Motion**

2692 In a synchrotron, the field  $B$  is varied during acceleration (a function performed  
 2693 by the power supply) concurrently with the variation of the bunch momentum  $p$  (a  
 2694 function performed by the accelerating cavity) in such a way that at any time

$$\Delta W = F \times 2\pi R = 2\pi q R \rho \dot{B} B(t) \rho = p(t)/q \quad (9.29)$$

so that the beam is maintained on the design orbit. Given the energies involved, the magnet supply imposes its law and the cavity follows  $B(t)$  (Fig. 9.11), the best it can. The accelerating voltage  $\hat{V}(t) = \sin \omega_{rf} t$  is maintained in synchronism with the

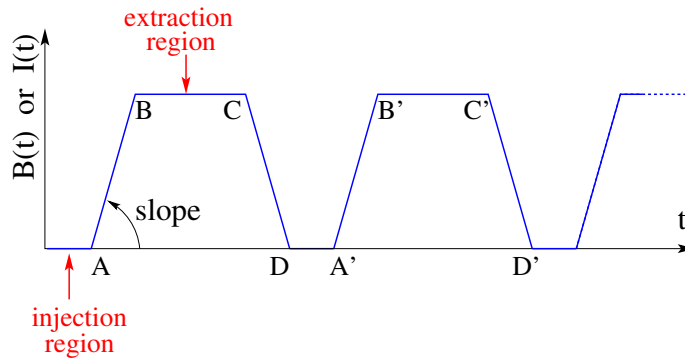


**Fig. 9.11** Cycling  $B(t)$  in a pulsed synchrotron. Ignoring saturation,  $B(t)$  is proportional to the magnet power supply current  $I(t)$ . Beam injection occurs at low field, in the region of A, extraction occurs at top energy, on the high field plateau. (AB): field ramp up (acceleration); (BC): flat top; (CD): field ramp down; (DA’): thermal relaxation. (AA’): repetition period; (1/AA’): repetition rate; *slope*: ramp velocity  $\dot{B} = dB/dt$  (Tesla/s).

revolution motion, its angular frequency satisfying

$$\omega_{\text{rf}} = h\omega_{\text{rev}} = h \frac{c}{R} \frac{B(t)}{\sqrt{\left(\frac{m_0}{q\rho}\right)^2 + B^2(t)}}$$

2695 *Energy gain*

2696 The variation of the particle energy over a turn amounts to the work of the force  
2697  $F = dp/dt$  on the charge at the cavity, namely

$$\Delta W = F \times 2\pi R = 2\pi q R \rho \dot{B} \quad (9.30)$$

Over most of the acceleration cycle in a slow-cycling synchrotron  $\dot{B}$  is usually constant (Eq. 9.3), thus so is  $\Delta W$ . At Saturne I for instance (the object of Exercise 9.1, parameters in Tab. 9.1)

$$\frac{\Delta W}{q} = 2\pi R \rho \dot{B} = 68.9 \times 8.42 \times 1.8 = 1044 \text{ volts}$$

The field ramp lasts

$$\Delta t = (B_{\text{max}} - B_{\text{min}})/\dot{B} \approx B_{\text{max}}/\dot{B} = 0.8 \text{ s}$$

The number of turns to the top energy ( $W_{\text{max}} \approx 3 \text{ GeV}$ ) is

$$N = \frac{W_{\text{max}}}{\Delta W} = \frac{3 \cdot 10^9 \text{ eV}}{1044 \text{ eV/turn}} \approx 3 \cdot 10^6 \text{ turns}$$

The dependence of particle mass on field writes

$$m(t) = \gamma(t)m_0 = \frac{q\rho}{c} \sqrt{\left(\frac{m_0}{qc\rho}\right)^2 + B(t)^2}$$

2698 *Adiabatic damping of the betatron oscillations*

The focusing index (Eq. 9.5) does not change during acceleration, thus the tunes  $\nu_x$  and  $\nu_y$  do not change either. As a result of the longitudinal acceleration at the cavity though, the longitudinal energy of the particles is modified. This results in a decrease of the amplitude of betatron oscillations (an increase if the cavity is decelerating). The mechanism is sketched in Fig. 9.12: the slope, respectively before and after (index 2) the cavity is

$$\frac{dx}{ds} = \frac{m \frac{dx}{dt}}{m \frac{ds}{dt}} = \frac{p_x}{p_s}, \quad \frac{dx}{ds} \Big|_2 = \frac{m \frac{dx}{dt}}{m \frac{ds}{dt}} \Big|_2 = \frac{p_{x,2}}{p_{s,2}}$$



Particle mass and velocity are modified at the traversal of the cavity but, as the

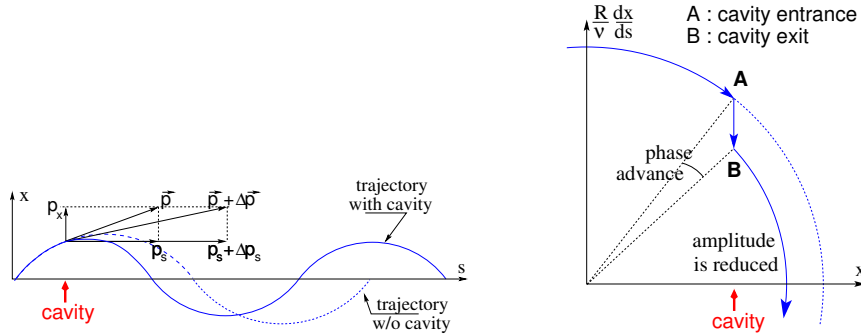


**Fig. 9.12** Adiabatic damping of betatron oscillations, here from  $x' = p_x/p_s$  before the cavity, to  $x'_2 = p_x/(p_s + \Delta p_s)$  after the cavity. In the horizontal phase space, to the right of decrease of  $\Delta\left(\frac{dx}{ds}\right)$  if  $\frac{dx}{ds} > 0$ , increase of  $\Delta\left(\frac{dx}{ds}\right)$  if  $\frac{dx}{ds} < 0$

force is longitudinal,  $dp_x/dt = 0$  thus  $p'_x = p_x$ , the increase in momentum is purely longitudinal,  $p'_s = p_s + \Delta p$ . Thus

$$\left. \frac{dx}{ds} \right|_2 = \frac{p_x}{p_s + \Delta p} \approx \frac{p_x}{p_s} \left(1 - \frac{\Delta p}{p_s}\right)$$

and as a consequence the slope  $dx/ds$  varies across the cavity,

$$\Delta\left(\frac{dx}{ds}\right) = \left. \frac{dx}{ds} \right|_2 - \frac{dx}{ds} = -\frac{dx}{ds} \frac{\Delta p_s}{p_s}$$

2699 The variation of the slope is proportional to the slope, with opposite sign if  $\Delta p/p > 0$   
 2700 (acceleration) thus a decrease of the slope. This variation has two consequences on  
 2701 the betatron oscillation (Fig. 9.12):  
 2702 - a change of the betatron phase,  
 2703 - a modification of the betatron amplitude.

2704 *Coordinate transport*

2705 at the cavity writes  $\begin{cases} x_2 = x \\ x'_2 \approx \frac{p_x}{p_s} \left(1 - \frac{dp}{p}\right) = x' \left(1 - \frac{dp}{p}\right) \end{cases}$ . In matrix form,  $\begin{pmatrix} x_2 \\ x'_2 \end{pmatrix} =$

2706  $[C] \begin{pmatrix} x \\ x' \end{pmatrix}$  with

$$[C] = \begin{bmatrix} 1 & 0 \\ 0 & 1 - \frac{dp}{p} \end{bmatrix} \tag{9.31}$$

2707 and  $\det[C] = 1 - \frac{dp}{p} \neq 1$ : the system is non-conservative, the surface of the beam  
 2708 ellipse in phase space is not conserved. Assume one cavity in the ring and note  
 2709  $[T] \times [C]$  the one-turn coordinate transport matrix with origin at entrance of the  
 2710 cavity. Its determinant is  $\det[T] \times \det[C] = \det[C] = 1 - \frac{dp}{p}$ ; the variation of  
 2711 the transverse ellipse surface satisfies  $\varepsilon_u = (1 - \frac{dp}{p_0})\varepsilon_0$  or, with  $d\varepsilon_u = \varepsilon_u - \varepsilon_0$ ,  
 2712  $\frac{d\varepsilon_u}{\varepsilon_u} = -\frac{dp}{p_0}$ , the solution of which is

$$p \varepsilon_u = \text{constant}, \text{ or } \beta\gamma\varepsilon_u = \text{constant} \quad (9.32)$$

2713 Over  $N$  turns the coordinate transport matrix is  $[T_N] = ([T][C])^N$ , its determinant  
 2714 is  $(1 - \frac{dp}{p})^N \approx 1 - N\frac{dp}{p}$ : the ellipse surface changes by that factor.

2715 *Synchrotron motion; phase stability*

2716 “Synchrotron motion” designates the mechanism of phase stability, or longitudinal  
 2717 focusing (Fig. 9.13), that stabilizes the longitudinal motion of a particle in the vicinity  
 2718 of a synchronous phase,  $\phi_s$ , in virtue of

2719 (i) the presence of an accelerating cavity with its frequency indexed on the  
 2720 revolution time,

2721 (ii) with the bunch centroid positioned either on the rising slope of the oscillating  
 2722 voltage (low energy regime), or on the falling slope (high energy regime).

The synchronous (or “ideal”) particle follows the equilibrium trajectory around  
 the ring (the reference closed orbit, about which all other particles will undergo a  
 betatron oscillation), its velocity satisfies  $v(t) = \frac{qB\rho(t)}{m}$ ; at each turn it reaches the  
 accelerating gap when the oscillating voltage is at the synchronous phase  $\phi_s$ , and  
 undergoes an energy gain

$$\Delta W = q\hat{V} \sin \phi_s$$

The condition  $|\sin \phi_s| < 1$  imposes a lower limit to the cavity voltage for acceleration  
 to happen, namely, after Eq. 9.30,

$$\hat{V} > 2\pi R\rho\dot{B}$$

2723 Referring to Fig. 9.13, the synchronous phase can be placed on the left (A A' A''...  
 2724 series in the Figure, or on the right (B B' B''... series) of the oscillating voltage crest.  
 2725 One and only one of these two possibilities, and which one depending upon the optical  
 2726 lattice and on particle energy, ensures that particles in a bunch remain grouped in  
 2727 the vicinity of the synchronous particle. The transition is between two time-of-flight  
 2728 regimes: a particle which gains momentum compared to the synchronous particle  
 2729 has a greater velocity, while

2730 - in the high bunch energy regime the increase in path length around the ring  
 2731 is faster than the increase in velocity (velocity essentially does not even change  
 2732 in ultrarelativistic regime), a revolution around the ring takes more time (this is the  
 2733 classical cyclotron and synchrocyclotron regime, and as well the high energy electron

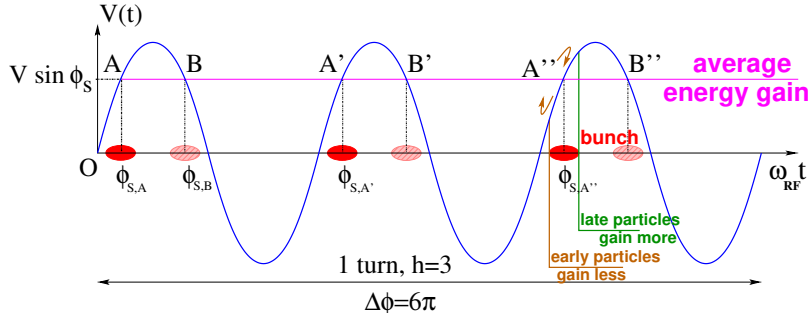


**Fig. 9.13** A sketch of the mechanism of phase stability,  $h = 3$  in this example. Below transition phase stability occurs for a synchronous phase taken at either one of A, A', A'' arrival times at the gap: a particle with higher energy goes around the ring more rapidly than the synchronous particle; if both are launched together, the former arrives earlier at the voltage gap (at  $\phi < \phi_{s,A}$ ) so experiencing weaker acceleration; at lower energy the particle is slower, it arrives at the gap later,  $\phi > \phi_{s,A}$ , so experiencing a greater voltage; this results in an overall stable oscillatory motion around the synchronous phase. Beyond transition the stable phase is at either one of B, B', B'' locations: a particle which is less energetic than the synchronous particle arrives earlier,  $\phi < \phi_{s,B}$ , so experiencing a greater voltage, and inversely, resulting in overall stable synchrotron motion.

2734 synchrotron regime); consider such a particle, arriving at the accelerating gap late  
 2735 ( $\phi(t) > \phi_s$ ), in order for it to be pulled toward bunch center (*i.e.*, take less time  
 2736 around the ring) it has to undergo deceleration; this is the B series, above transition;  
 2737 - in the low bunch energy regime velocity increase is faster than path length  
 2738 increase, thus a revolution around the ring is faster; consider such a particle, arriving  
 2739 at the accelerating gap early ( $\phi(t) < \phi_s$ ), in order for it to be pulled toward bunch  
 2740 center (*i.e.*, take more time around the ring) it has to be slowed down, it has to  
 2741 undergo deceleration; this is the A series, below transition.

2742 *Transition energy*

2743 The transition between the two time-of-flight regimes occurs at  $\frac{dT_{\text{rev}}}{T_{\text{rev}}} = 0$ . With  
 2744  $T = 2\pi/\omega = C/v$ , this can be written  $\frac{d\omega_{\text{rev}}}{\omega_{\text{rev}}} = -\frac{dT_{\text{rev}}}{T_{\text{rev}}} = \frac{dv}{v} - \frac{dC}{C}$ . With  $\frac{dv}{v} = \frac{1}{\gamma^2} \frac{dp}{p}$   
 2745 and momentum compaction  $\alpha = \frac{dC}{C} / \frac{dp}{p}$ , (Eq. 9.28), this can be written

$$\frac{d\omega_{\text{rev}}}{\omega_{\text{rev}}} = -\frac{dT_{\text{rev}}}{T_{\text{rev}}} = \left( \frac{1}{\gamma^2} - \alpha \right) \frac{dp}{p} = \eta \frac{dp}{p} \quad (9.33)$$

2746 wherein the phase-slip factor has been introduced,

$$\eta = \overbrace{\frac{1}{\gamma^2}}^{\text{kinematics}} - \underbrace{\alpha}_{\text{lattice}} = \frac{1}{\gamma^2} - \frac{1}{\gamma_{\text{tr}}^2} \quad (9.34)$$

2747 The transition  $\gamma$  appears to be a property of the lattice.

2748 In a weak focusing lattice  $\gamma_{\text{tr}} = 1/\sqrt{\alpha} \approx \nu_x$  (Eqs. 4.20, 9.28), thus the phase  
2749 stability regime is

$$\begin{aligned} &\text{below transition, i.e. } \phi_s < \pi/2, \quad \text{if } \gamma < \nu_x \\ &\text{above transition, i.e. } \phi_s > \pi/2, \quad \text{if } \gamma > \nu_x \end{aligned} \quad (9.35)$$

2750 In a weak focusing synchrotron the horizontal tune  $\nu_x = \sqrt{(1-n)R/\rho_0}$  (Eq. 9.25)  
2751 may be  $\geq 1$ , and subsequently  $\gamma_{\text{tr}} > 1$  is a possibility. There is no transition-gamma  
2752 if  $\nu_x < 1$ . Acceleration to 3 GeV in Saturne I for instance, from 50 MeV at injection,  
2753 and with  $\nu_x \approx 0.7$  (Tab. 9.1) did not require transition-gamma crossing<sup>3</sup>.

### 2754 9.1.2 Spin Motion, Depolarizing Resonances

2755 The field index is essentially zero in the ZGS, transverse focusing is ensured by  
2756 wedge angles at the ends of the height dipoles, which is thus the only location where  
2757 non-zero horizontal field components are found. As a consequence depolarizing  
2758 resonances are weak: “As we can see from the table, the transition probability [from  
2759 spin state  $\psi_{1/2}$  to spin state  $\psi_{-1/2}$ ] is reasonably small up to  $\gamma = 7.1$ ” [13], i.e.  
2760  $G\gamma = 12.73$ ,  $p = 6.6$  GeV/c; the table referred to stipulates a transition probability  
2761  $P_{\frac{1}{2}, -\frac{1}{2}} < 0.042$ , whereas resonances beyond that energy range feature  $P_{\frac{1}{2}, -\frac{1}{2}} > 0.36$ .  
2762 Beam depolarization up to 6 GeV/c, under the effect of these resonances, is illustrated  
2763 in Fig. 9.14.

2764 In a synchrotron using gradient dipoles, particles experience radial fields all along  
2765 the latter as they undergo vertical betatron oscillations, as an effect of the radial field  
2766 index [13, 20, 21]. However these radial field components are weak, and so is there  
2767 effect on spin motion as long as the particle energy is low enough (an effect of the  $\gamma$   
2768 factor in the spin precession Eq. 4.28, Chap. 4).

Assuming a defect-free ring, the vertical betatron motion excites “intrinsic” spin  
resonances, located at

$$G\gamma_R = k P \pm \nu_y$$

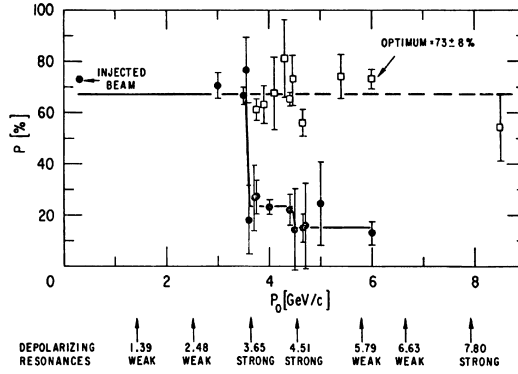
with  $k$  an integer and  $P$  the period of the ring. In the ZGS for instance,  $\nu_y \approx 0.8$   
(Tab. 9.2), the ring is  $P=4$ -periodic, thus  $G\gamma_R = 4k \pm 0.8$ . Strongest resonances are  
located at

<sup>3</sup> Transition-gamma crossing, or “gamma jump”, is a common beam manipulation during acceleration in strong focusing synchrotrons, it requires an RF phase jump, the technique is addressed in Chapter 10.

$$G\gamma_R = mkP \pm \nu_y$$

2769 with  $m$  the number of cells per superperiod [22, Sec. 3.II]. In the ZGS,  $m=2$  thus  
 2770 strongest resonances occur at  $G\gamma_R = 2 \times 4k \pm 0.8 = 7.2$  ( $p = 3.65$  GeV/c), 8.8  
 (4.51 GeV/c), 15.2 (7.9 GeV/c), ... (Fig. 9.14).

**Fig. 9.14** Depolarizing intrinsic resonance landscape up to 9 GeV/c at the ZGS (solid circles) [23]. Systematic resonances are located at  $G\gamma_R = 4 \times \text{integer} \pm \nu_y$ , stronger ones at  $G\gamma_R = 8 \times \text{integer} \pm \nu_y$ . A tune jump was applied to preserve polarization when crossing strong resonances (empty circles)



2771

In the presence of vertical orbit defects, non-zero periodic transverse fields are experienced along the closed orbit, they excite “imperfection” depolarizing resonances, located at

$$G\gamma_R = k$$

with  $k$  an integer. In the case of systematic defects the periodicity of the orbit is that of the lattice,  $P$ , imperfection resonances are located at  $G\gamma_R = kP$ . Strongest imperfection resonances are located at [22, Sec. 3.II]

$$G\gamma_R = mkP$$

2772 Crossing a depolarizing resonance of strength  $\epsilon_R$  causes a loss of polarization  
 2773 given by (Froissart-Stora formula [24])

$$\frac{P_f}{P_i} = 2e^{-\frac{\pi}{2} \frac{|\epsilon_R|^2}{\alpha}} - 1 \quad (9.36)$$

2774 from a value  $P_i$  upstream to an asymptotic value  $P_f$  downstream of the resonance.  
 2775 This assumes an isolated resonance, crossed at an energy gain  $\Delta E$  per turn, with a  
 2776 crossing speed

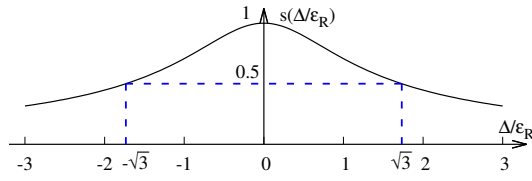
$$\alpha = G \frac{d\gamma}{d\theta} = \frac{1}{2\pi} \frac{\Delta E}{M} \quad (9.37)$$

2777 *Spin precession axis. Resonance width*

2778 Consider the spin vector  $\mathbf{S}(\theta) = (S_\eta, S_\xi, S_y)$  of a particle in the laboratory frame,  
2779 with  $\theta$  the orbital angle around the accelerator. Introduce the projection  $s(\theta)$  of  $\mathbf{S}$   
2780 in the median plane

$$s(\theta) = S_\eta(\theta) + jS_\xi(\theta) \quad (\text{and } S_y^2 = 1 - s^2) \quad (9.38)$$

**Fig. 9.15** Modulus of the horizontal spin component.  $s = 1/2$  at distance  $\Delta = \pm\sqrt{3}\epsilon_R$  from  $G\gamma_R$



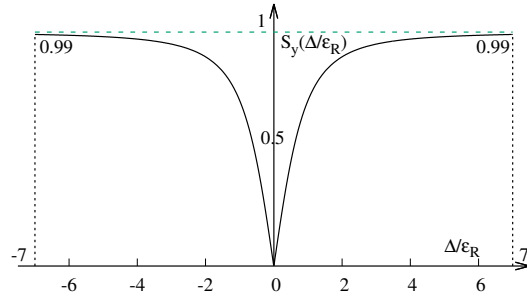
2781

2782 It can be shown that in the case of a stationary solution of the spin motion, viz.  
2783 the spin precession axis,  $s$  satisfies [21] (Fig. 9.15)

$$s^2 = \frac{1}{1 + \frac{\Delta^2}{|\epsilon_R|^2}} \quad (9.39)$$

with  $\Delta = G\gamma - G\gamma_R$  the distance to the resonance. The resonance width is a measure

**Fig. 9.16** Dependence of polarization on the distance to the resonance. For instance  $S_y = 0.99$ , 1% depolarization, corresponds to  $\Delta = 7|\epsilon_R|$ . On the resonance,  $\Delta = 0$ , the precession axis lies in the median plane,  $S_y = 0$



2784

2785 of its strength (Fig. 9.16). The quantity of interest is the angle,  $\phi$ , of the spin  
2786 precession direction to the vertical axis, given by (Fig. 9.16)

$$\cos \phi(\Delta) \equiv S_y(\Delta) = \sqrt{1 - s^2} = \frac{\Delta/|\epsilon_R|}{\sqrt{1 + \Delta^2/|\epsilon_R|^2}} \quad (9.40)$$

2787 On the resonance,  $\Delta = 0$ , the spin precession axis lies in the bend plane:  $\phi = \pm\pi/2$ .  
 2788  $S_y = 0.99$  (1% depolarization) corresponds to a distance to the resonance  $\Delta = 7|\epsilon_R|$ ,  
 2789 spin precession axis at an angle  $\phi = \text{acos}(0.99) = 8^\circ$  from the vertical.  
 2790 Conversely, given  $S_y$ ,

$$\frac{\Delta^2}{|\epsilon_R|^2} = \frac{S_y^2}{1 - S_y^2} \tag{9.41}$$

The precession axis is common to all spins,  $S_y$  is a measure of the polarization along the vertical axis,

$$S_y = \frac{N^+ - N^-}{N^+ + N^-}$$

2791 wherein  $N^+$  and  $N^-$  denote the number of particles in spin states  $\frac{1}{2}$  and  $-\frac{1}{2}$  respectively.  
 2792

2793 *Spin motion through weak resonances*

Depolarizing resonances are weak up to several GeV in a weak focusing synchrotron, as the radial and/or longitudinal fields, which stem from a small radial field index and from dipole fringe fields, are weak. Spin motion  $S_y(\theta)$  through a resonance in that case can be assumed to satisfy  $S_{y,f} \approx S_{y,i}$ , with  $S_{y,f}$  and  $S_{y,i}$  the asymptotic vertical spin component values respectively upstream and downstream of the resonance). As a consequence it can be calculated in terms of the Fresnel integrals [20, 21]

$$C(x) = \int_0^x \cos\left(\frac{\pi}{2}t^2\right) dt, \quad S(x) = \int_0^x \sin\left(\frac{\pi}{2}t^2\right) dt$$

namely, with the origin of the orbital angle is taken at the resonance (Fig. 9.17),

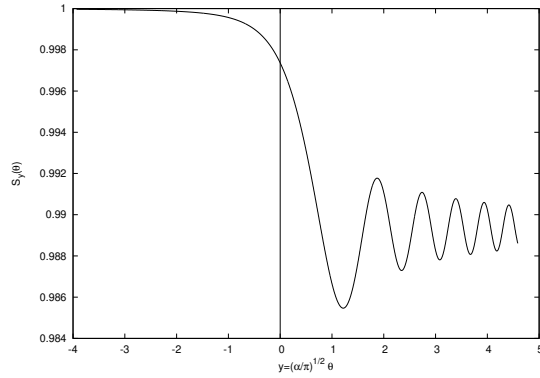


**Fig. 9.17** Vertical component of spin motion  $S_y(\theta)$  through a weak depolarizing resonance (after Eq. 9.42). The vertical bar is at the location of the resonance, which coincides with the origin of the orbital angle

$$\begin{aligned}
 \text{if } \theta < 0 : \left( \frac{S_y(\theta)}{S_{y,i}} \right)^2 &= 1 - \frac{\pi}{\alpha} |\epsilon_R|^2 \left\{ \left[ 0.5 - C \left( -\theta \sqrt{\frac{\alpha}{\pi}} \right) \right]^2 + \left[ 0.5 - S \left( -\theta \sqrt{\frac{\alpha}{\pi}} \right) \right]^2 \right\} \\
 \text{if } \theta > 0 : \left( \frac{S_y(\theta)}{S_{y,i}} \right)^2 &= 1 - \frac{\pi}{\alpha} |\epsilon_R|^2 \left\{ \left[ 0.5 + C \left( \theta \sqrt{\frac{\alpha}{\pi}} \right) \right]^2 + \left[ 0.5 + S \left( \theta \sqrt{\frac{\alpha}{\pi}} \right) \right]^2 \right\}
 \end{aligned}$$

2795 In the asymptotic limit,

$$\frac{S_y(\theta)}{S_{y,i}} \xrightarrow{\theta \rightarrow \infty} 1 - \frac{\pi}{\alpha} |\epsilon_R|^2 \quad (9.43)$$

2796 which identifies with the development of Froissart-Stora formula  $P_f/P_i =$

2797  $2 \exp\left(-\frac{\pi}{2} \frac{|\epsilon_R|^2}{\alpha}\right) - 1$  to the first order in  $|\epsilon_R|^2/\alpha$ . This approximation holds in the  
 2798 limit that higher order terms can be neglected:  $|\epsilon_R|^2/\alpha \ll 1$ .

## 2799 9.2 Exercises

### 2800 9.1 Construct Saturne I synchrotron. Spin Resonances

2801 Solution: page 346

2802 In this exercise, Saturne I synchrotron is modeled in `zgoubi`, and spin resonances  
 2803 in a weak focusing gradient synchrotron are studied.

2804 (a) Construct a model of Saturne I 90° cell dipole in the hard-edge model, using  
 2805 DIPOLE. Use parameters given in Tab. 9.1, and Fig. 9.18 as a guidance. Take an  
 2806 integration step size in centimeter range - check convergence as you proceed. In  
 2807 order to allow beam monitoring, split the dipole in two 45° deg halves. It is judicious  
 2808 (although in no way a necessity) to take RM=841.93 cm in DIPOLE.

2809 Find the 6 × 6 transport matrix of that dipole. MATRIX can be used for that, with  
 2810 OBJET[KOBJ=5] to define a proper set of initial coordinates.

2811 Check against theory (refer to Sect. 18.2, Eq. 18.31).

2812 (b) Construct a model of Saturne I cell, with origin at the center of the drift. Take  
 2813 the reference orbit along the arc of nominal radius in the dipoles, 841.93 cm.

2814 Compute the tunes using MATRIX; check their values against theory.

2815 Move the origin along the drift, verify that, while the cell matrix depends on the  
 2816 origin, its trace does not change.

2817 Produce a scan of the tunes over the field index range  $0.5 \leq n \leq 0.757$ . RE-  
 2818 BELOTE can be used to repeatedly change  $n$  over that range. Superimpose the  
 2819 theoretical curves  $\nu_x(n)$ ,  $\nu_y(n)$ .

2820 Using TWISS and OBJET[KOBJ=5], produce the periodic beam matrix of the  
 2821 cell. TWISS causes a print out of both the transport matrix and the periodic beam  
 2822 matrix: check that these satisfy Eq. 19.14.

2823 (c) Launch 60 particles evenly distributed on a common paraxial horizontal  
 2824 Courant-Snyder invariant (vertical motion is taken null). Store particle data along  
 2825 the ring in `zgoubi.plt`, using DIPOLE[IL=2] and DRIFT[split,N=20,IL=2]. Use these  
 2826 to produce a graph of  $x^2(s) / \epsilon_x / \pi$ .



2827 From this graph, get the value of the betatron function  $\beta_x$  at the ends of the cell,  
 2828 compare with TWISS outcomes. Find the minimum and maximum values of the  
 2829 beta functions, and their azimuth  $s(\min[\beta_x])$ ,  $s(\max[\beta_x])$ . Check the latter against  
 2830 theory.

2831 Repeat for the vertical motion, taking  $\varepsilon_x = 0$ ,  $\varepsilon_y$  paraxial.

2832 (d) Answer the previous question using, instead of 60 particles, a single particle  
 2833 traced over a few tens of turns.

2834 (e) Find the closed orbit for an off-momentum particle. FIT can be used for that.  
 2835 From the raytracing outcomes, produce a graph of the dispersion function  $D_x(s)$ .

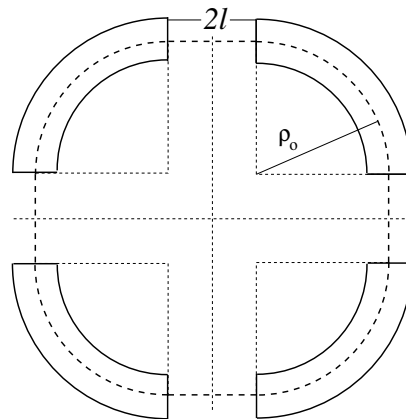


**Fig. 9.18** A schematic layout of Saturne I, a  $2\pi/4$  axial symmetry structure, comprised of 4 radial field index 90 deg dipoles and 4 drift spaces. The cell in the simulation exercises is taken as a  $\pi/4$  quadrant: l-drift/90°-dipole/l-drift

**Table 9.1** Parameters of Saturne 1 weak focusing synchrotron [25].  $\rho_0$  denotes the reference bending radius in the dipole; the reference orbit, field index, wave numbers, etc., are taken along that radius

Orbit length, $C$	cm	6890
Average radius, $R = C/2\pi$	cm	1096.58
Straight section length, $2l$	cm	400
Magnetic radius, $\rho_0$	cm	841.93
$R/\rho_0$		1.30246
Field index $n$ , nominal value		0.6
Wave numbers, $\nu_x; \nu_y$		0.724; 0.889 **** verif wrt. simul
Stability limit		$0.5 < n < 0.757$
Injection energy	MeV	3.6
Field at injection	kG	0.0326
Top energy	GeV	2.94
$\dot{B}$	T/s	1.8
Field at top energy, $B_{\max}$	kG	14.9
$B_{\max}\rho$	T m	13
Field ramp at injection	kG/s	20
Synchronous energy gain	keV/turn	1.160
RF harmonic		2

(f) Justify considering the betatron oscillation as sinusoidal, namely,

$$y(\theta) = A \cos(\nu_y \theta + \phi)$$

2836 wherein  $\theta = s/R$ ,  $R = \oint ds/2\pi$ .

2837 Find the value of the horizontal and vertical betatron functions, resulting from  
2838 that approximation. Compare with the betatron functions obtained in (b).

2839 (g) Produce an acceleration cycle from 3.6 MeV to 3 GeV, for a few particles  
2840 launched on a common  $10^{-4} \pi\text{m}$  initial invariant in each plane. Ignore synchrotron  
2841 motion (CAVITE[IOPT=3] can be used in that case). Take a peak voltage  $\hat{V} = 200 \text{ kV}$   
2842 (unrealistic though, as it would result in a nonphysical  $\dot{B}$  (Eq. 9.30)) and synchronous  
2843 phase  $\phi_s = 150 \text{ deg}$  (justify  $\phi_s > \pi/2$ ).

2844 Check the accuracy of the betatron damping over the acceleration range, compared  
2845 to theory.

2846 How close to symplectic the numerical integration is (it is by definition *not*  
2847 symplectic, being a truncated Taylor series method [26, Eq. 1.2.4]), depends on the  
2848 integration step size, and on the size of the flying mesh in the DIPOLE method [26,  
2849 Fig. 20]; check a possible departure of the betatron damping from theory as a function  
2850 of these parameters.

2851 Produce a graph of the the evolution of the horizontal and vertical wave numbers  
2852 during the acceleration cycle.

2853 (h) Change the peak voltage to  $\hat{V} = 20 \text{ kV}$ . Produce a graph of the value of the  
2854 vertical spin component of the particles as a function of  $G\gamma$ , over the acceleration  
2855 range from 3.6 MeV to 3 GeV. Adding SPNTRK will ensure spin tracking.

2856 Produce a graph of the average value of  $S_Z$  over that 200 particle set, as a function  
2857 of  $G\gamma$ . Indicate on that graph the location of the resonant  $G\gamma_R$  values.

2858 (i) Based on the simulation file used in (f), simulate the acceleration of a single  
2859 particle, through the intrinsic resonance  $G\gamma_R = 4 - \nu_Z$ , from a few thousand turns  
2860 upstream to a few thousand turns downstream.

2861 Perform this resonance crossing for five different values of the particle invariant,  
2862 namely:  $\varepsilon_Z/\pi = 2, 10, 20, 40, 200 \mu\text{m}$ .

2863 Compute  $P_f/P_i$  in each case, check the dependence on  $\varepsilon_Z$  against theory. Com-  
2864 pute the resonance strength in each case, check the dependence on  $\varepsilon_Z$  against theory.

2865 Re-do this crossing simulation for a different crossing speed (take for instance  
2866  $\hat{V} = 10 \text{ kV}$ ) and a couple of vertical invariant values, compute  $P_f/P_i$  so obtained.  
2867 Check the crossing speed dependence of  $P_f/P_i$  against theory.

2868 (j) Produce a graph of the turn-by-turn vertical spin component motion  $S_Z(\text{turn})$   
2869 across the resonance  $G\gamma_R = 4 - \nu_Z$ , in a weakly depolarizing case,  $P_f \approx P_i$ . Show  
2870 that it satisfies Eq. 9.42. Match the data to the latter to get the vertical betatron tune  
2871  $\nu_y$ , and the location of the resonance  $G\gamma_R$ .

2872 (k) Track a few particles at fixed energy, at distances from the resonance  $G\gamma_R =$   
2873  $4 - \nu_y$  of up to a  $7 \times \varepsilon_R$  (this distance corresponds to 1% depolarization).

2874 Produce on a common graph the spin motion  $S_Z(\text{turn})$  for all these particles, as  
2875 observed at some azimuth along the ring.

2876 Produce a graph of  $\langle S_y \rangle|_{\text{turn}}(\Delta)$  (as in Fig. 9.16).

Produce the vertical betatron tune  $\nu_y$ , and the location of the resonance  $G\gamma_R$ , obtained from a match of these tracking trials to the theoretical (Eq. 9.40)

$$\langle S_y \rangle (\Delta) = \frac{\Delta}{\sqrt{|\epsilon_R|^2 + \Delta^2}}$$

2877 **9.2 Construct the ZGS synchrotron. Spin Resonances**

2878 Solution: page 371

2879 In this exercise, ZGS synchrotron is modeled in zgoubi, and spin resonances in  
2880 this weak focusing zero-gradient synchrotron are studied.

2881 (a) Construct an approximate model of the ZGS synchrotron, using DIPOLE.  
2882 Use Figs. 9.19, 9.20 as a guidance, and parameters given in Tab. 9.2. Assume that  
2883 the reference orbit is the same at all energies, on nominal radius, 2076 cm. It is  
2884 judicious (although in no way an obligation) to take RM=2076 in DIPOLE. (Note  
2885 that in reality, unlike the present assumption for this exercise, the reference orbit in  
2886 ZGS moved outward during acceleration [27].)

2887 Validate the model by producing the lattice parameters of the ring. TWISS can  
2888 be used for that. Compare with the lattice parameters given in Tab. 9.2.

2889 (b) Produce a graph of the betatron functions along the ZGS cell.

2890 Check the radial distance between on- and off-momentum closed orbits obtained  
2891 from raytracing, against Eq. 9.27. Provide a graph of the dispersion function.

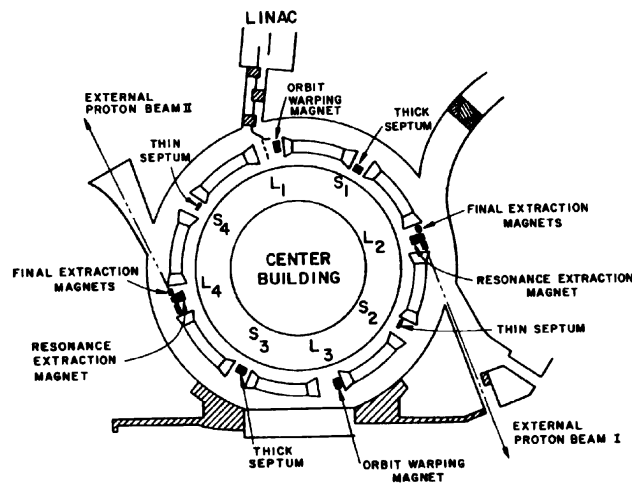


**Fig. 9.19** A schematic layout of the ZGS [23], a  $\pi/2$ -periodic structure, comprised of 8 zero-index dipoles, 4 long and 4 short straight sections

2892 (c) Additional verifications regarding the model.

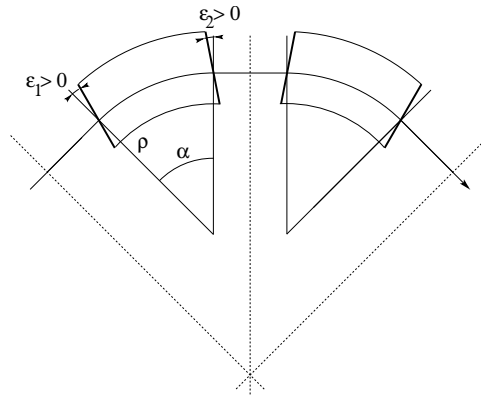


**Fig. 9.20** A sketch of ZGS cell layout. In defining the entrance and exit faces (EFBs) of the magnet, beam goes from left to right. Wedge angles at the long straight sections ( $\varepsilon_1$ ) and at the short straight sections ( $\varepsilon_2$ ) are different

**Table 9.2** Parameters of the ZGS weak focusing synchrotron after Refs. [27, 28] [23, pp.288-294,p. 716] (2nd column, when they are known) and in the present simplified model and numerical simulations (3rd column). Note that the actual orbit is skewed (moves) during ZGS acceleration cycle, tunes change as well - this is not the case in the present modeling

		From Refs. [27, 28]	Simplified model
Injection energy	MeV		50
Top energy	GeV		12.5
$G\gamma$ span			1.888387 - 25.67781
Length of central orbit	m	171.8	170.90457
Length of straight sections, total	m	41.45	40.44
<i>Lattice</i>			
Wave numbers $\nu_x; \nu_y$		0.82; 0.79	0.849; 0.771
Max. $\beta_x; \beta_y$	m		32.5; 37.1
<i>Magnet</i>			
Length	m	16.3	16.30486 (magnetic)
Magnetic radius	m	21.716	20.76
Field min.; max.	kG	0.482; 21.5	0.4986; 21.54
Field index			0
Yoke angular extent	deg	43.02590	45
Wedge angle	deg	$\approx 10$	13 and 8
<i>RF</i>			
Rev. frequency	MHz	0.55 - 1.75	0.551 - 1.751
RF harmonic $h=\omega_{rf}/\omega_{rev}$			8
Peak voltage	kV	20	200
B-dot, nominal/max.	T/s	2.15/2.6	
Energy gain, nominal/max.	keV/turn	8.3/10	100
Synchronous phase, nominal	deg		150
<i>Beam</i>			
$\varepsilon_x; \varepsilon_y$ (at injection)	$\pi \mu\text{m}$		25; 150
Momentum spread, rms			$3 \times 10^{-4}$
Polarization at injection	%	$> 75$	100
Radial width of beam (90%), at inj.	inch	2.5	$\sqrt{\beta_x \varepsilon_x / \pi} = 1.1$

2893 Produce a graph of the field  $B(s)$   
 2894 - along the on-momentum closed orbit, and along off-momentum chromatic closed  
 2895 orbits, across a cell;  
 2896 - along orbits at large horizontal excursion;  
 2897 - along orbits at large vertical excursion.  
 2898 For all these cases, verify qualitatively, from the graphs, that  $B(s)$  appears as  
 2899 expected.

(d) Justify considering the betatron oscillation as sinusoidal, namely,

$$y(\theta) = A \cos(\nu_y \theta + \phi)$$

2900 wherein  $\theta = s/R$ ,  $R = \oint ds/2\pi$ .

2901 Find the value of the horizontal and vertical betatron functions, resulting from  
 2902 that approximation. Compare with the betatron functions obtained in (b).

2903 (e) Produce an acceleration cycle from 50 MeV to 17 GeV about, for a few particles  
 2904 launched on a common  $10^{-5} \pi\text{m}$  vertical initial invariant, with small horizontal  
 2905 invariant. Ignore synchrotron motion (CAVITE[IOPT=3] can be used in that case).  
 2906 Take a peak voltage  $\hat{V} = 200 \text{ kV}$  (this is unrealistic but yields 10 times faster  
 2907 computing than the actual  $\hat{V} = 20 \text{ kV}$ , Tab. 9.2) and synchronous phase  $\phi_s = 150 \text{ deg}$   
 2908 (justify  $\phi_s > \pi/2$ ). Add spin, using SPNTRK, in view of the next question, (f).

2909 Check the accuracy of the betatron damping over the acceleration range, compared  
 2910 to theory. How close to symplectic the numerical integration is (it is by definition  
 2911 *not* symplectic), depends on the integration step size, and on the size of the flying  
 2912 mesh in the DIPOLE method [26, Fig. 20]; check a possible departure of the betatron  
 2913 damping from theory as a function of these parameters.

2914 Produce a graph of the the evolution of the horizontal and vertical wave numbers  
 2915 during the acceleration cycle.

2916 (f) Using the raytracing material developed in (e): produce a graph of the vertical  
 2917 spin component of the particles, and the average value over that 200 particle set, as  
 2918 a function of  $G\gamma$ . Indicate on that graph the location of the resonant  $G\gamma_R$  values.

2919 (g) Based on the simulation file used in (f), simulate the acceleration of a single  
 2920 particle, through one particular intrinsic resonance, from a few thousand turns  
 2921 upstream to a few thousand turns downstream.

2922 Perform this resonance crossing for different values of the particle invariant.  
 2923 Determine the dependence of final/initial vertical spin component value, on the  
 2924 invariant value; check against theory.

2925 Re-do this crossing simulation for a different crossing speed. Check the crossing  
 2926 speed dependence of final/initial vertical spin component so obtained, against theory.

2927 (h) Introduce a vertical orbit defect in the ZGS ring.

2928 Find the closed orbit.

2929 Accelerate a particle launched on that closed orbit, from 50 MeV to 17 GeV about,  
 2930 produce a graph of the vertical spin component.

2931 Select one particular resonance, reproduce the two methods of (g) to check the  
 2932 location of the resonance at  $G\gamma_R = \text{integer}$ , and to find its strength.

## 2933 References

- 2934 1. Veksler, V.: A new method of acceleration of relativistic particles. J. of Phys. USSR 9 153-158  
 2935 (1945)
- 2936 2. McMillan, E. M.: The Synchrotron. Phys. Rev. 68 143-144 (1945)
- 2937 3. Goward, F. K., and Barnes, D. E.: Experimental 8 MeV synchrotron for electron acceleration.  
 2938 Nature 158, 413 (1946)
- 2939 4. Richardson, J.R., et al.: Frequency Modulated Cyclotron. Phys. Rev. 69: 669 (1946)
- 2940 5. Kerst, D. W.: The Acceleration of Electrons by Magnetic Induction.. Phys. Rev., 60, 47-53  
 2941 (1941)
- 2942 6. Photo saturne I. \*\*\*\*\* TB completed \*\*\*\* Archives historiques CEA. Copyright  
 2943 CEA/Service de documentation - FAR\_SA\_N\_00248
- 2944 7. Photo tranche dipole. Credit: CEA Saclay. \*\*\*\*\* TB completed \*\*\*\*\*  
 2945 Archives historiques CEA. Copyright CEA/Service de documentation - FAR\_SA\_N\_02826
- 2946 8. Sessler, A., Wilson, E.: Engines of Discovery. A Century of Particle Accelerators. World  
 2947 Scientific, 2007
- 2948 9. \*\*\*\*\* fnal loma linda synch copyrights \*\*\*\*\*
- 2949 10. Endo, K., et al.: Compact proton and carbon ion synchrotrons for radiation therapy. MOPRI087,  
 2950 Proceedings of EPAC 2002, Paris, France; pp. 2733-2735.  
 2951 <https://accelconf.web.cern.ch/e02/PAPERS/MOPRI087.pdf>
- 2952 11. Vostrikov, V.A., et al.: Novel approach to design of the compact proton synchrotron magnetic  
 2953 lattice. tupsa17, 26th Russian Particle Accelerator Conference RUPAC2018, Protvino, Russia  
 2954 (2018).  
 2955 <https://accelconf.web.cern.ch/rupac2018/papers/tupsa17.pdf>
- 2956 12. Cohen, D. : Feasibility of Accelerating Polarized Protons with the Argonne ZGS. Review of  
 2957 Scientific Instruments 33, 161 (1962)// <https://doi.org/10.1063/1.1746524>
- 2958 13. Ratner, L.G. and Khoe, T.K.: Acceleration of Polarized Protons in the Zero Gradient Syn-  
 2959 chrotron. Procs. PAC 1973 Conference, Washington (1973).  
 2960 [http://accelconf.web.cern.ch/p73/PDF/PAC1973\\_0217.PDF](http://accelconf.web.cern.ch/p73/PDF/PAC1973_0217.PDF)
- 2961 14. Cho, Y., et als.: Effects of depolarizing resonances on a circulating beam of polarized protons  
 2962 during or storage in a synchrotron. IEEE Trans. Nuclear Science, Vol.NS-24, No.3, June 1977

- 2963 15. Parker, E.F.: High Energy Polarized Deuterons at the Argonne National Laboratory Zero  
2964 Gradient Synchrotron. IEEE Transactions on Nuclear Science, Vol. NS-26, No. 3, June 1979,  
2965 pp 3200-3202
- 2966 16. Leleux, G.: Accélérateurs Circulaires. Lecture Notes, INSTN, CEA Saclay (1978)
- 2967 17. Suddeth, D.E., et als.: Pole face winding equipment for eddy current correction at the Zero  
2968 Gradient Synchrotron. Procs. PAC 1973 Conference, Washington (1973).  
2969 [http://accelconf.web.cern.ch/p73/PDF/PAC1973\\_0397.PDF](http://accelconf.web.cern.ch/p73/PDF/PAC1973_0397.PDF)
- 2970 18. Rauchas, A.V. and Wright, A.J.: Betatron tune profile control in the Zero Gradient Synchrotron  
2971 (ZGS) using the main magnet pole face windings. Procs. PAC1977 conference, IEEE Trans.  
2972 on Nucl. Science, VoL.NS-24, No.3, June 1977
- 2973 19. Floquet, G.: Sur les équations différentielles linéaires à coefficients périodiques. Annales  
2974 scientifiques de l'E.N.S. 2e série, tome 12 (1883), p. 47-88.  
2975 [http://www.numdam.org/item?id=ASENS\\_1883\\_2\\_12\\_47\\_0](http://www.numdam.org/item?id=ASENS_1883_2_12_47_0)
- 2976 20. Leleux, G.: Traversée des résonances de dépolarisation. Rapport Interne LNS/GT-91-15,  
2977 Saturne, Groupe Théorie, CEA Saclay (février 1991)
- 2978 21. Méot, F.: Spin Dynamics. Polarized Beam Dynamics and Instrumentation in Particle Accelerators: USPAS Summer 2021 Spin Class Lectures, Springer (2023)
- 2979 22. Lee, S.Y.: Spin Dynamics and Snakes in Synchrotrons. World Scientific, 1997
- 2980 23. Khoe, T.K., et al.: The High Energy Polarized Beam at the ZGS. Procs. IXth Int. Conf on  
2981 High Energy Accelerators, Dubna, pp. 288-294 (1974).
- 2982 24. Froissart, M. and Stora, R.: Dépolarisation d'un faisceau de protons polarisés dans un synchrotron. Nucl. Inst. Meth. 7 (1960) 297.
- 2983 25. Bruck H., Debraine P., Levy-Mandel R., Lutz J., Podliasky I., Prevot F., Taieb J., Winter S.D.,  
2984 Maillet R., Caractéristiques principales du Synchrotron à Protons de Saclay et résultats obtenus  
2985 lors de la mise en route, rapport CEA no.93, CEN-Saclay, 1958.
- 2986 26. Méot, F.: Zgoubi Users' Guide.  
2987 <https://www.osti.gov/biblio/1062013-zgoubi-users-guide> Sourceforge latest version:  
2988 <https://sourceforge.net/p/zgoubi/code/HEAD/tree/trunk/guide/Zgoubi.pdf>
- 2989 27. Foss, M.H., et al.: The Argonne ZGS Magnet. IEEE 1965, pp. 377-382, June 1965
- 2990 28. Klaisner, L.A., et al.: IEEE 1965, pp. 133-137, June 1965